


# PHOTONICS Research

## Highly luminescent and stable lead-free cesium copper halide perovskite powders for UV-pumped phosphor-converted light-emitting diodes

LINGLING XIE,<sup>1,†</sup> BINGKUN CHEN,<sup>2,\*†</sup> FA ZHANG,<sup>2</sup> ZIHENG ZHAO,<sup>2</sup> XINXIN WANG,<sup>1</sup> LIJIE SHI,<sup>1</sup> YUE LIU,<sup>2</sup> LINGLING HUANG,<sup>2</sup>  RUIBIN LIU,<sup>1,4</sup> BINGSUO ZOU,<sup>1</sup> AND YONGTIAN WANG<sup>2,3</sup>

<sup>1</sup>Beijing Key Laboratory of Nanophotonics and Ultrafine Optoelectronic Systems, School of Physics, Beijing Institute of Technology, Beijing 100081, China

<sup>2</sup>Beijing Engineering Research Center of Mixed Reality and Advanced Display, School of Optics and Photonics, Beijing Institute of Technology, Beijing 100081, China

<sup>3</sup>AICFVE of Beijing Film Academy, Beijing 100088, China

<sup>4</sup>e-mail: liusir@bit.edu.cn

\*Corresponding author: chenbk@bit.edu.cn

Received 14 January 2020; revised 20 February 2020; accepted 10 March 2020; posted 13 March 2020 (Doc. ID 387707); published 6 May 2020

Lead halide perovskites have drawn extensive attention over recent decades owing to their outstanding photoelectric performances. However, their toxicity and instability are big issues that need to be solved for further commercialization. Herein, we adopt a facile dry ball milling method to synthesize lead-free  $\text{Cs}_3\text{Cu}_2\text{X}_5$  ( $\text{X} = \text{I}, \text{Cl}$ ) perovskites with photoluminescence (PL) quantum yield up to 60%. The optical features including broad emission spectrum, large Stokes shift, and long PL lifetime can be attributed to self-trapped exciton recombination. The as-synthesized blue emissive  $\text{Cs}_3\text{Cu}_2\text{I}_5$  and green emissive  $\text{Cs}_3\text{Cu}_2\text{Cl}_5$  lead-free perovskite powders have good thermal stability and photostability. Furthermore, UV-pumped phosphor-converted light-emitting diodes were obtained by using  $\text{Cs}_3\text{Cu}_2\text{I}_5$  and  $\text{Cs}_3\text{Cu}_2\text{Cl}_5$  as phosphors. © 2020 Chinese Laser Press

<https://doi.org/10.1364/PRJ.387707>

### 1. INTRODUCTION

Metal-halide perovskite materials have attracted significant attention over the past decades owing to their advantages of high absorption coefficient, large carrier diffusion lengths, and superior photoelectric properties [1–4], which make them promising candidates for optoelectronic applications including solar cells [5–7], light-emitting diodes [8–14], photodetectors [15,16], and lasers [17–19]. Unfortunately, toxicity and poor stability are major obstacles that restrict their significant commercialization [20,21]. It is highly necessary to develop lead-free perovskite materials to solve these issues. So far, many efforts have been made to explore lead-free all-inorganic compounds through searching for low- or non-toxic elements to replace lead, including tin (Sn) [22–26], bismuth (Bi) [27–29], silver (Ag) [30,31], indium (In) [32,33], antimony (Sb) [34,35], germanium (Ge) [36,37], copper (Cu) [38–44], zinc (Zn) [45], magnesium (Mg) [46], and rare-earth ions [47]. Among these rising lead-free perovskite materials, cesium copper halide perovskites benefit from being low cost and earth abundant. In previous reports, a limited number of synthetic methods have been used to fabricate cesium copper halide perovskites, which depend on solvents with low recovery rates, causing a certain degree of environmental pollution [48].

Sustainable development of solvent-free technologies for the synthesis of cesium copper halide perovskites has become a critical issue.

The ball milling approach based on mechanochemistry, a kind of green and reemerging efficient synthetic method, was identified by the International Union of Pure and Applied Chemistry (IUPAC) as one of 10 world-changing technologies [49]. The process can promote physical and chemical reactions between solids quickly and quantitatively with no added solvent, consistent with sustainable development. Moreover, the ball milling method offers tremendous advantages compared to traditional solution-based methods by avoiding the solubility limitation for poorly soluble or insoluble reagents and achieving high yield in a relatively short time by controlling materials [50]. Recently, it has been adopted to fabricate lead halide perovskite materials [51,52]. However, there are no reports to our knowledge about using the ball milling approach to fabricate cesium copper halide perovskites. In this work, we first extended the ball milling method to prepare highly luminescent and stable  $\text{Cs}_3\text{Cu}_2\text{I}_5$  and  $\text{Cs}_3\text{Cu}_2\text{Cl}_5$  perovskite powders without solvent. The as-fabricated all-inorganic copper-based perovskites exhibit self-trapped excitons (STE) emission features including broad photolumines-

cent (PL) emission, large Stokes shift, long PL lifetime, and high PL quantum yield (QY) reaching 60%. The  $\text{Cs}_3\text{Cu}_2\text{I}_5$  and  $\text{Cs}_3\text{Cu}_2\text{Cl}_5$  perovskites with good thermal stability and photostability were employed as phosphors for UV-pumped phosphor-converted (pc)-LEDs.

## 2. EXPERIMENT

### A. Materials and Synthesis

The materials used were cesium iodide (CsI, 99.9% metal basis, Aladdin), cuprous iodide (CuI, 99.9% metal basis, Aladdin), cesium chloride (CsCl, 99.5%, Macklin), and cuprous (I) chloride (CuCl, 99.5%, Macklin). All chemicals were used as received without further purifications.  $\text{Cs}_3\text{Cu}_2\text{X}_5$  powders were fabricated by the dry ball milling method at room temperature. In typical synthesis of  $\text{Cs}_3\text{Cu}_2\text{I}_5$  powder, 3 mmol CsI (0.779 g) and 2 mmol CuI (0.38 g) were first homogeneously mixed in a mortar; the mixture was then transferred into a grinding tank (steel bowl with steel ball, 10 mL). The sealed tank was installed in the vibratory ball mill, and the gray-white  $\text{Cs}_3\text{Cu}_2\text{I}_5$  powder was obtained by grinding at 1000 r/min for half an hour. For the synthesis of  $\text{Cs}_3\text{Cu}_2\text{Cl}_5$  powder, CsI and CuI were simply replaced by CsCl and CuCl in the same process.

### B. Fabrication of UV-Pumped pc-LEDs

0.05 g of  $\text{Cs}_3\text{Cu}_2\text{I}_5$  powder and 0.05 g of  $\text{Cs}_3\text{Cu}_2\text{Cl}_5$  powder were mixed with a thermal-curable silicone resin OE-6551A (0.1 g) under vigorous stirring. The hardener OE-6551B (0.2 g) was added to form a fluorescent paste, and then the paste was deposited on a commercial GaN-based UV-LED chip (310 nm, EPILED Co., Ltd).

### C. Characterization

The morphologies and elemental analysis of  $\text{Cs}_3\text{Cu}_2\text{I}_5$  and  $\text{Cs}_3\text{Cu}_2\text{Cl}_5$  were collected by scanning electron microscope (SEM), energy dispersive X-ray (EDX, FEI Quanta FEG 250 ESEM), and transmission electron microscope (TEM) (JEOL, JEM-2010F, 200 kV) equipped with an X-ray spectrometer detector. X-ray diffraction (XRD) patterns of  $\text{Cs}_3\text{Cu}_2\text{I}_5$  and  $\text{Cs}_3\text{Cu}_2\text{Cl}_5$  powders were recorded on an X-ray diffractometer (Bruker AXS D8) using  $\text{Cu-K}\alpha$  X-ray radiation ( $\lambda = 1.5406 \text{ \AA}$ ). Thermogravimetric analysis (TGA) results of the powder were obtained using a PerkinElmer Diamond TG/DTA6300, conducted at a heating rate of  $10^\circ\text{C} \cdot \text{min}^{-1}$  to  $1500^\circ\text{C}$  in  $\text{N}_2$  flow with an alumina crucible. X-ray photoelectron spectroscopy (XPS) measurements were performed on a ULVAC-PHI instrument (PHIQUAN-TERA-II SXM) with  $\text{Al K}\alpha$  as the X-ray source at 70 W. The UV-Vis diffuse reflectance spectra of the powdered samples were taken on a PerkinElmer Lambda 35 double-beam spectrometer. PL and PL excitation (PLE) spectra were recorded on the Horiba PTI QuantaMaster 400. The absolute PL QY's time-resolved PL decay curves were measured on an FLSP920 spectrofluorimeter (Edinburgh Instruments, TCSPC system) equipped with an integrating sphere.

### D. Computational Methods

First-principle calculations of  $\text{Cs}_3\text{Cu}_2\text{I}_5$  were carried out using the Vienna Ab initio Simulation Package (VASP) code. To guarantee convergence, the projected augmented plane wave basis set was defined by a cutoff of 300 eV. The mesh samplings

in the Brillouin zone (BZ) were  $3 \times 3 \times 2$ . Experimental lattice parameters of  $\text{Cs}_3\text{Cu}_2\text{I}_5$  were used, and the atomic positions were fully relaxed until the residual forces were  $0.05 \text{ eV/\AA}$ . Electronic band structures, density of states (DOS), and exciton properties were calculated using the hybrid PBE0 function.

## 3. RESULTS AND DISCUSSION

The schematic procedure of a typical fabrication of  $\text{Cs}_3\text{Cu}_2\text{I}_5$  powder by using a planetary ball mill is illustrated in Fig. 1(a): the raw powder materials of cesium iodide (CsI) and cuprous iodide (CuI) were first homogeneously mixed in a mortar; the mixture was then transferred into a steel bowl with a steel ball, and the blue emissive product was generated after a grinding process of the mixture for half an hour at room temperature, demonstrating an extremely energy-saving procedure compared to previous reports on lead perovskites [51–53]. The SEM image of the  $\text{Cs}_3\text{Cu}_2\text{I}_5$  powder is shown in Fig. 1(b), and it exhibits irregularly shaped particles with the diameter of  $0.71 \pm 0.3 \text{ }\mu\text{m}$ , consistent with the TEM result [Fig. 1(c)]. The high-resolution TEM (HRTEM) image [Fig. 1(d)] of the  $\text{Cs}_3\text{Cu}_2\text{I}_5$  powder shows high crystallinity with a lattice fringe of  $0.38 \text{ nm}$  corresponding to the crystal plane (022). The high crystallinity feature also can be confirmed by the selected area electron diffraction (SAED) pattern as shown in the inset of Fig. 1(d). EDX measurement [Fig. 1(e)] was performed

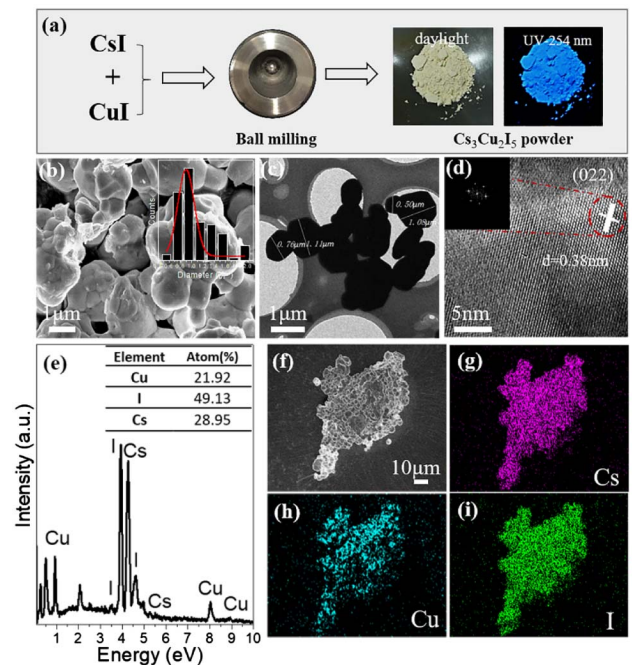


**Fig. 1.** (a) Schematic illustration of synthetic process of  $\text{Cs}_3\text{Cu}_2\text{I}_5$  perovskite powder by using a planetary ball mill. (b) SEM image of  $\text{Cs}_3\text{Cu}_2\text{I}_5$  perovskite powder with inset showing size distribution. (c) TEM image of  $\text{Cs}_3\text{Cu}_2\text{I}_5$  perovskite. (d) HRTEM image of  $\text{Cs}_3\text{Cu}_2\text{I}_5$  perovskite along with an inset of SAED pattern of  $\text{Cs}_3\text{Cu}_2\text{I}_5$  perovskite crystal. (e) EDX spectrum and elemental content analysis of obtained  $\text{Cs}_3\text{Cu}_2\text{I}_5$  perovskite. (f) SEM image and EDX elemental mapping (g) Cs, (h) Cu, and (i) I of the selected  $\text{Cs}_3\text{Cu}_2\text{I}_5$  perovskite powder.

to estimate the chemical composition of  $\text{Cs}_3\text{Cu}_2\text{I}_5$  powder sample, which yielded a Cs:Cu:I ratio of  $\approx 3:2:5$ , indicating that the  $\text{Cs}_3\text{Cu}_2\text{I}_5$  compound was successfully synthesized. Elemental mapping of the product has been performed to further confirm the presence of Cs, Cu, and I in the resulting  $\text{Cs}_3\text{Cu}_2\text{I}_5$  powder as shown in Figs. 1(f)–1(i), exhibiting the homogeneous distribution of three elements over the particles.

We performed XRD measurement to verify the phase structure of the as-synthesized  $\text{Cs}_3\text{Cu}_2\text{I}_5$ ; as shown in Fig. 2(a), the XRD patterns with main  $2\theta$  positions of  $13.1^\circ$ ,  $15.1^\circ$ ,  $23.9^\circ$ ,  $25.6^\circ$ ,  $26.3^\circ$ ,  $28.2^\circ$ ,  $30.6^\circ$ , and  $47.9^\circ$  were assigned to the (111), (002), (122), (312), (222), (131), (313), and (152) planes of a bulk  $\text{Cs}_3\text{Cu}_2\text{I}_5$  (JCPDS No. 45-0077). These results indicate that the as-fabricated  $\text{Cs}_3\text{Cu}_2\text{I}_5$  powder has a orthorhombic crystal structure with a space group of  $Pnma$ , consistent with previous reports [40]. The stability of  $\text{Cs}_3\text{Cu}_2\text{I}_5$  perovskite is a critical factor for its applications, and thus TGA was carried out to investigate the thermal stability of the  $\text{Cs}_3\text{Cu}_2\text{I}_5$  powder. Figure 2(b) shows that the as-synthesized  $\text{Cs}_3\text{Cu}_2\text{I}_5$  powder is stable to  $560^\circ\text{C}$ , indicating that it has a good thermal stability, much better than that of Sn-based perovskite [24]. The valence state and surface chemical composition of  $\text{Cs}_3\text{Cu}_2\text{I}_5$  were reaffirmed from XPS. The XPS survey spectrum [Fig. 2(c)] confirms the presence of Cs, Cu, and I elements. Figures 2(d)–2(f) show the high-resolution XPS (HRXPS) spectra of Cs 3d, Cu 2p, and I 3d for the  $\text{Cs}_3\text{Cu}_2\text{I}_5$  powder sample, and all spectra were calibrated with C 1 s. The HRXPS spectrum peaks of Cs 3d are located at 724.2 eV and 738.5 eV corresponding to  $\text{Cs}^+ 3d_{5/2}$  and  $3d_{3/2}$ ; the peaks at 619.0 eV and 930.6 eV for the I 3d XPS spectrum are attributed to  $\text{I}^- 3d_{5/2}$  and  $3d_{3/2}$ , respectively. The binding energies of 932.2 eV and 952.1 eV were observed in the Cu 2p XPS spectrum for Cu 2p $_{1/2}$  and 2p $_{3/2}$ , respectively, which demonstrates the existence of  $\text{Cu}^+$  [41].

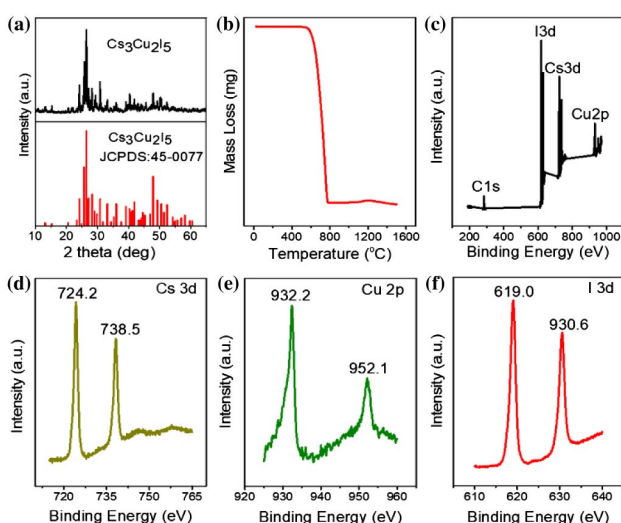


**Fig. 2.** (a) XRD pattern of obtained  $\text{Cs}_3\text{Cu}_2\text{I}_5$  powder, compared with the orthorhombic bulk  $\text{Cs}_3\text{Cu}_2\text{I}_5$  at the bottom (JCPDS No. 45-0077). (b) TGA curve of  $\text{Cs}_3\text{Cu}_2\text{I}_5$  powder. (c) XPS survey spectrum and HRXPS spectra of (d) Cs 3d, (e) Cu 2p, and (f) I 3d in  $\text{Cs}_3\text{Cu}_2\text{I}_5$  powder.

The absolute PL QY of  $\text{Cs}_3\text{Cu}_2\text{I}_5$  was measured up to 60%, indicating that our sample has a strong emission feature. Figure 3(a) shows PL spectra of  $\text{Cs}_3\text{Cu}_2\text{I}_5$  powder under different excitation wavelengths ranging from 260 to 340 nm, with a uniform full width at half-maximum (FWHM) of 80 nm. Figure 3(b) predicts the PLE spectra of  $\text{Cs}_3\text{Cu}_2\text{I}_5$  with a fixed peak at 303 nm, which makes it suitable as phosphor for UV-pumped pc-LEDs. The large Stokes shift of 137 nm between the PLE and PL peaks illustrates that the emission mechanism cannot be explained simply by a direct band recombination emission [54,55]. UV-Vis optical diffuse reflectance spectroscopy was adopted to determine the optical bandgap of  $\text{Cs}_3\text{Cu}_2\text{I}_5$  powder as shown in Fig. 3(c), featuring a sharp absorption band centered at 324 nm. A bandgap value of 3.69 eV was given through the Tauc plot [inset of Fig. 3(c)]. To further explore excitonic recombination kinetics, the time-resolved PL decay curve of  $\text{Cs}_3\text{Cu}_2\text{I}_5$  powder was measured under 300 nm excitation as shown in Fig. 3(d). The PL decay can be described by monoexponential fitting, giving a long-lived PL lifetime of 1.13  $\mu\text{s}$  that exhibits the phosphorescence feature of  $\text{Cs}_3\text{Cu}_2\text{I}_5$ . Summarizing the optical features of the  $\text{Cs}_3\text{Cu}_2\text{I}_5$  sample, including a broad PL spectrum, a large Stokes shift, and a long PL decay time, we can deduce that the emission of  $\text{Cs}_3\text{Cu}_2\text{I}_5$  is ascribed to the STE recombination mechanism due to the Jahn–Teller distortion of the polyhedron (formed by  $\text{Cu}^+$  and  $\text{I}^-$ ) in the excited states [33,56]. The electronic structure calculations were performed using density functional theory (DFT) to further study the fluorescence mechanism of the  $\text{Cs}_3\text{Cu}_2\text{I}_5$  powder, first giving the crystal structure of the  $\text{Cs}_3\text{Cu}_2\text{I}_5$  as viewed down the  $a$  axis [Fig. 3(e)] consisting of caged  $[\text{Cu}_2\text{I}_5]^{3-}$  units with tetrahedral and trigonal  $\text{Cu}^+$  sites, isolated by  $\text{Cs}^+$  ions. Figure 3(f) provides the density of states (DOS) of the  $\text{Cs}_3\text{Cu}_2\text{I}_5$  sample, indicating that the valence band maximum (VBM) is mainly composed of Cu 3d orbits, while the conduction band maximum (CBM) originates from Cu 4s and I 5p orbits, and  $\text{Cs}^+$  has no contribution to CBM or VBM [40]. This means that the  $[\text{Cu}_2\text{I}_5]^{3-}$  polyhedron plays the dominant role in the crystal distortion and emission mechanism of  $\text{Cs}_3\text{Cu}_2\text{I}_5$ , which can confine the excitons trapped by Jahn–Teller distortion in excited states. This is consistent with the previous reports [40,54]. Additionally, DFT calculations also yielded that  $\text{Cs}_3\text{Cu}_2\text{I}_5$  crystal has a direct bandgap at the  $\Gamma$  point with the gap value of 3.70 eV [Fig. 3(g)]. The excitation and emission processes for  $\text{Cs}_3\text{Cu}_2\text{I}_5$  are described in Fig. 3(h): after excitation with a high-energy ultraviolet light, the electron moves first from the ground states to the excited states, and then transits from singlet to triplet states (self-trapped states). Subsequent transition of the electron from the STE states to the ground states occurs, accompanied by blue emission.

The thermal stability and photostability of perovskite materials are critical for their long-term application in lightings and displays. To evaluate the natural stability of  $\text{Cs}_3\text{Cu}_2\text{I}_5$  powder, the evolution of the PL spectra of  $\text{Cs}_3\text{Cu}_2\text{I}_5$  powder after thermal treatment under  $\text{N}_2$  protection at different temperatures ( $100^\circ\text{C}$ ,  $200^\circ\text{C}$ ,  $300^\circ\text{C}$ ) was tested for half an hour. It can be seen clearly from Fig. 4(a) that the PL intensity of the  $\text{Cs}_3\text{Cu}_2\text{I}_5$  powder shows no decrease for  $100^\circ\text{C}$  and  $200^\circ\text{C}$

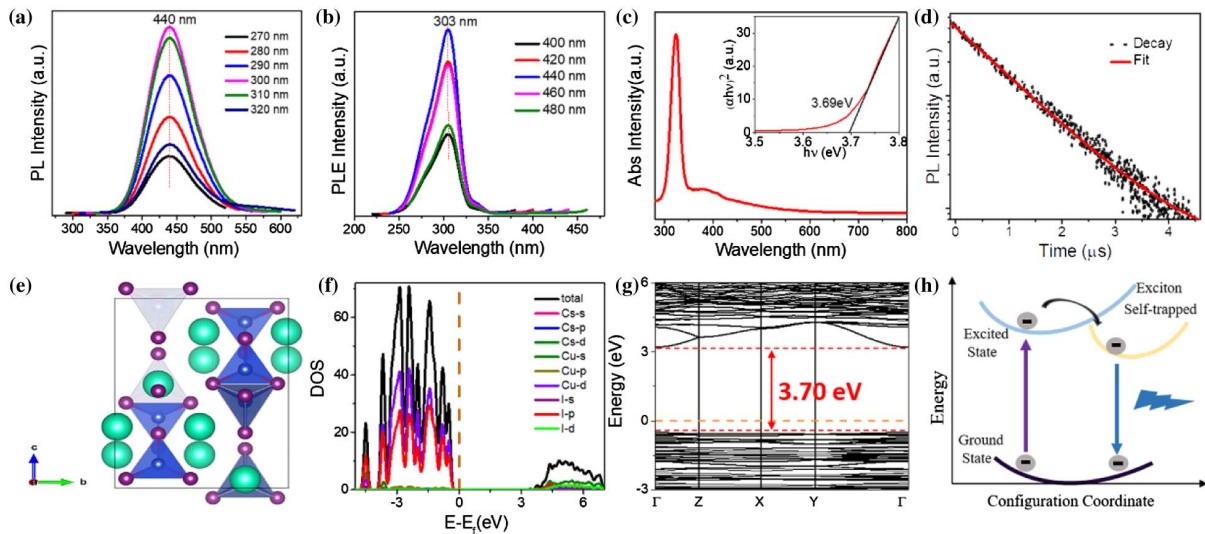


**Fig. 3.** (a) PL spectra of  $\text{Cs}_3\text{Cu}_2\text{I}_5$  powder under different excitation wavelengths from 260 to 340 nm. (b) PLE spectra measured at different PL peaks ranging from 400 to 480 nm. (c) UV-Vis diffuse reflectance spectrum of the  $\text{Cs}_3\text{Cu}_2\text{I}_5$  powder; the inset shows the Tauc plot used for the bandgap estimation. (d) Time-resolved PL decay curve of  $\text{Cs}_3\text{Cu}_2\text{I}_5$  powder excited by the laser of 300 nm. (e) Crystal structure of  $\text{Cs}_3\text{Cu}_2\text{I}_5$ , as viewed down the  $a$  axis (green, purple, and blue balls indicate Cs, I, and Cu atoms, respectively). (f) DOS plots of the  $\text{Cs}_3\text{Cu}_2\text{I}_5$  powder. (g) Calculated electronic band structure of  $\text{Cs}_3\text{Cu}_2\text{I}_5$ ; the Fermi energy is set to  $E = 0$  and denoted with an orange dash line. (h) Configuration coordinate diagram for the excited-state reorganization; the violet and blue arrows represent transition and radiation processes, respectively, and the black arrow represents intersystem crossing.

and only 21% reduction for 300°C compared to original value. Then the thermal stability of  $\text{Cs}_3\text{Cu}_2\text{I}_5$  powder was tested at 100°C under ambient air environment. The emission intensity remained at 72% of the initial value after 5 h [Fig. 4(b)], indicating that  $\text{Cs}_3\text{Cu}_2\text{I}_5$  powder has a good thermal stability [57]. The photostability of  $\text{Cs}_3\text{Cu}_2\text{I}_5$  powder was also studied [Fig. 4(c)] using a 500 W xenon lamp as the excitation source; the sample only exhibited a 22% reduction in PL intensity after 5 h illumination, which is better than Pb-based perovskites [58]. Interestingly, the  $\text{Cs}_3\text{Cu}_2\text{I}_5$  powder had a remarkable stability in air; the XRD patterns of a  $\text{Cs}_3\text{Cu}_2\text{I}_5$  powder exposed to ambient conditions for three months were identical to that of

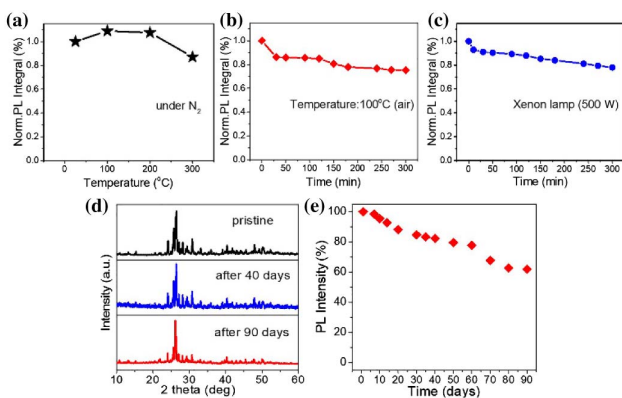


**Fig. 4.** (a) Integrated PL intensity as a function of temperatures from 25°C to 300°C. Variation of PL intensity of  $\text{Cs}_3\text{Cu}_2\text{I}_5$  (b) at 100°C and (c) under a xenon lamp irradiation over time. (d) XRD patterns of  $\text{Cs}_3\text{Cu}_2\text{I}_5$  exposed to air for three months. (e) PL intensity of  $\text{Cs}_3\text{Cu}_2\text{I}_5$  exposed to air for three months.

the initial as-synthesized powder [Fig. 4(d)]. PL intensity remained at 60% of the initial value after 90 days [Fig. 4(e)], much better than that of other reported perovskites [28,42,59]. The reason for the high stability of the as-fabricated  $\text{Cs}_3\text{Cu}_2\text{I}_5$  perovskite is most likely that there are no organic species (organic ions and ligands) contained in its structure and surface [60–62].

Notably, green emissive  $\text{Cs}_3\text{Cu}_2\text{Cl}_5$  perovskite was achieved for the first time to our knowledge. The SEM image is shown in Fig. 5(a), and it exhibits irregularly shaped micrometer-sized particles of the obtained  $\text{Cs}_3\text{Cu}_2\text{Cl}_5$ . Figure 5(b) shows the HRTEM image of the  $\text{Cs}_3\text{Cu}_2\text{Cl}_5$ , indicating high crystallinity with a lattice fringe of 0.35 nm. The SAED pattern of the  $\text{Cs}_3\text{Cu}_2\text{Cl}_5$  [inset of Fig. 5(b)] further confirms the high crystallinity. EDX elemental mappings of the selected  $\text{Cs}_3\text{Cu}_2\text{Cl}_5$  particles [Fig. 5(c)] showcase the uniform distribution of cesium, copper, and chlorine elements in the particles. The XRD pattern [Fig. 5(d)] shows that the diffraction peak positions and corresponding intensities are mainly consistent with the bulk  $\text{Cs}_3\text{Cu}_2\text{Cl}_5$  standard card (JCPDS No. 24-0247). The  $\text{Cs}_3\text{Cu}_2\text{Cl}_5$  exhibits an orthorhombic phase structure with the lattice constants  $a = 9.176 \text{ \AA}$ ,  $b = 10.505 \text{ \AA}$ , and  $c = 13.141 \text{ \AA}$ . We found that an additional  $\text{CsCl}$  phase signal appeared in the XRD pattern, which is marked with black stars; it is unavoidable for synthesis of chloride compounds [39,63]. The existing three elements were further confirmed by XPS results as shown in Fig. 5(e). The HRXPS analysis [Figs. 5(f) and 5(g)] of the Cs 3d (3d<sub>5/2</sub>, 724.2 eV; 3d<sub>3/2</sub>, 738.5 eV) and Cl 2p (198.3 eV) reveals that monovalent  $\text{Cs}^+$  and monovalent  $\text{Cl}^-$  existed in the  $\text{Cs}_3\text{Cu}_2\text{Cl}_5$  sample [9,64], while the HRXPS spectrum of Cu 2p [Fig. 5(h)] provides two main peaks of monovalent  $\text{Cu}^+$  (932.6 eV, 953.2 eV) with two

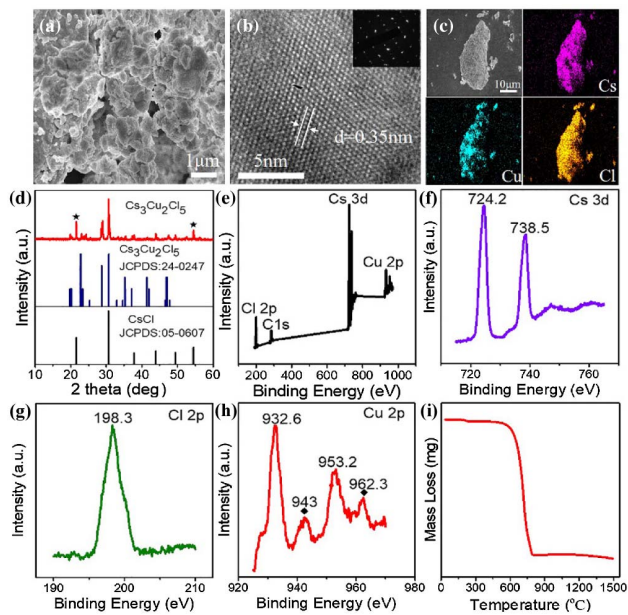


**Fig. 5.** (a) SEM image of  $\text{Cs}_3\text{Cu}_2\text{Cl}_5$  perovskite powder. (b) HRTEM image of  $\text{Cs}_3\text{Cu}_2\text{Cl}_5$  perovskite along with an inset of SAED pattern of  $\text{Cs}_3\text{Cu}_2\text{Cl}_5$  perovskite crystal. (c) EDX elemental mappings of  $\text{Cs}_3\text{Cu}_2\text{Cl}_5$  powder; the scale bar is 10  $\mu\text{m}$ . (d) XRD pattern of  $\text{Cs}_3\text{Cu}_2\text{Cl}_5$  powder with standard JCPDS cards ( $\text{Cs}_3\text{Cu}_2\text{Cl}_5$ , 24-0247 and  $\text{CsCl}$ , 05-0607). (e) XPS survey spectrum of  $\text{Cs}_3\text{Cu}_2\text{Cl}_5$  powder. HRXPS analysis of  $\text{Cs}_3\text{Cu}_2\text{Cl}_5$  powder: (f) Cs 3d spectrum, (g) Cl 2p spectrum, and (h) Cu 2p spectrum. (i) TGA curve of  $\text{Cs}_3\text{Cu}_2\text{Cl}_5$  powder.

satellite peaks (marked with black diamonds) at 942.4 eV and 962.3 eV attributed to divalent  $\text{Cu}^{2+}$  [65]. This may be because of the slight oxidation of partial  $\text{Cu}^+$  on the surface of the sample. The stability of  $\text{Cs}_3\text{Cu}_2\text{Cl}_5$  is further illustrated by the TGA result [Fig. 5(i)], which shows that the product is stable to 500°C, indicating that it displays a good thermal stability.

The UV-Vis absorption and PL spectra of  $\text{Cs}_3\text{Cu}_2\text{Cl}_5$  powder are depicted in Fig. 6(a), showing peaks at 346 nm for UV-Vis and 510 nm for PL. The broad PL spectrum (FWHM of 90 nm) of  $\text{Cs}_3\text{Cu}_2\text{Cl}_5$  makes it suitable for downconversion white pc-LEDs with high color rendering index. The optical photograph [inset of Fig. 6(a)] shows green color emission of the  $\text{Cs}_3\text{Cu}_2\text{Cl}_5$  powder under a UV-254 nm lamp. The normalized PLE spectra [Fig. 6(b)] exhibit identical shapes and fixed peaks, illustrating that the green emission of  $\text{Cs}_3\text{Cu}_2\text{Cl}_5$  originates from the relaxation of the same excited state [54]. A large Stokes shift of 164 nm between the PL and PLE spectra further makes it a candidate for use in pc-LEDs. The time-resolved PL decay curve [Fig. 6(c)] under 300 nm excitation at room temperature for  $\text{Cs}_3\text{Cu}_2\text{Cl}_5$  perovskite powder shows biexponential behavior with an average lifetime of 103  $\mu\text{s}$  by integrating two individual lifetimes of 73.61  $\mu\text{s}$  (29%) and 116.4  $\mu\text{s}$  (71%), which is longer than that of  $\text{Cs}_3\text{Cu}_2\text{I}_5$  perovskite. The long PL lifetime is commonly known as phosphorescence originated from STEs [33,39]. Mott and Stoneham reported that the STE lifetime is related to the energy barrier that is required to be conquered for STE formation [66]. The

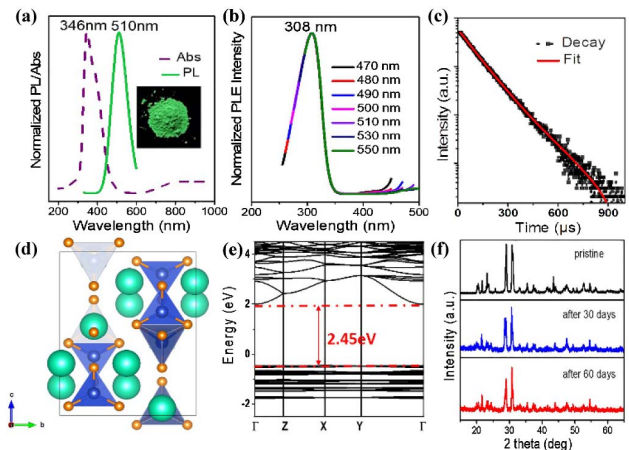


**Fig. 6.** (a) Normalized UV-Vis absorption (purple dash line) and PL (green solid line) spectra of the as-obtained  $\text{Cs}_3\text{Cu}_2\text{Cl}_5$  powder; inset: green emission image under UV-254 nm lamp. (b) Normalized PLE spectra measured over different PL peaks ranging from 470 to 550 nm. (c) Time-resolved PL decay curve of the  $\text{Cs}_3\text{Cu}_2\text{Cl}_5$  powder detected at 510 nm with excitation of 300 nm. (d) Crystal structure of  $\text{Cs}_3\text{Cu}_2\text{Cl}_5$ , as viewed down the  $a$  axis (green, brown, and blue balls indicate Cs, Cl, and Cu atoms, respectively). (e) DFT electronic band structure of  $\text{Cs}_3\text{Cu}_2\text{Cl}_5$  with a direct bandgap (2.45 eV). (f) XRD patterns of  $\text{Cs}_3\text{Cu}_2\text{Cl}_5$  exposed to air for two months.

potential barrier should be lower for  $\text{Cs}_3\text{Cu}_2\text{I}_5$  compared to  $\text{Cs}_3\text{Cu}_2\text{Cl}_5$ , which may explain the shorter relaxation time for excitons in  $\text{Cs}_3\text{Cu}_2\text{I}_5$  compared to that for excitons in  $\text{Cs}_3\text{Cu}_2\text{Cl}_5$ . It is consistent with the reported one [67]. The crystal structure of  $\text{Cs}_3\text{Cu}_2\text{Cl}_5$  powder is similar to  $\text{Cs}_3\text{Cu}_2\text{I}_5$  crystal, containing unique  $[\text{Cu}_2\text{Cl}_5]^{3-}$  dimers made of a trigonal planar  $\text{CuCl}_3$  sharing an edge with a tetrahedral  $\text{CuCl}_4$  unit, all surrounded by  $\text{Cs}^+$  [Fig. 6(d)]. And the electrons and phonons of  $\text{Cs}_3\text{Cu}_2\text{Cl}_5$  are strongly coupled to induce Jahn–Teller distortion of polyhedron  $[\text{Cu}_2\text{Cl}_5]^{3-}$  under UV light excitation. The excited-state electrons become self-trapped by the distortion and then release energy by a recombination process, and a similar emission behavior was also observed for other 0D lead-free crystal [68]. DFT calculations confirm that  $\text{Cs}_3\text{Cu}_2\text{Cl}_5$  has a direct bandgap at the  $\Gamma$  point with the value of 2.45 eV [Fig. 6(e)]. Furthermore, the absolute PL QY of  $\text{Cs}_3\text{Cu}_2\text{Cl}_5$  powder was measured up to 53%. The stability of the  $\text{Cs}_3\text{Cu}_2\text{Cl}_5$  powder was also studied in air conditions at room temperature by detecting variations of XRD patterns and PL intensity for 60 days. The XRD patterns [Fig. 6(f)] of  $\text{Cs}_3\text{Cu}_2\text{Cl}_5$  powder exhibit no changes; the PL intensity remained at 70% of the initial value, indicating that  $\text{Cs}_3\text{Cu}_2\text{Cl}_5$  powder also has better stability than other reported perovskites [28,42,59].

In order to illustrate the potential lighting application of the obtained perovskite powders, we fabricated a UV-pumped pc-LED device by using blue emissive  $\text{Cs}_3\text{Cu}_2\text{I}_5$  and green emissive  $\text{Cs}_3\text{Cu}_2\text{Cl}_5$  as phosphors. It is the first time to our knowledge that pc-LED based on all copper-based perovskites without other phosphors has been prepared. Figure 7(a) provides a photograph of the as-fabricated pc-LED with brown

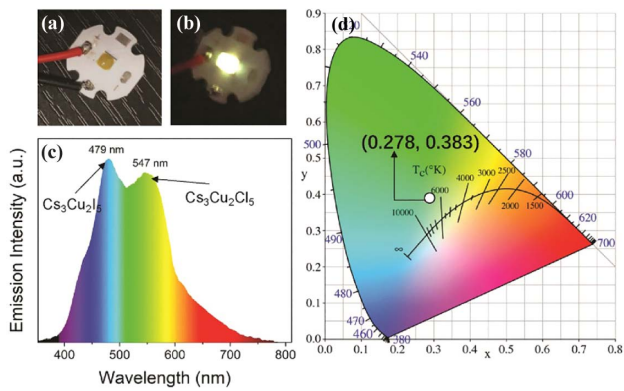


**Fig. 7.** (a) Photograph of the as-fabricated pc-LED based on dual phosphors of blue emissive  $\text{Cs}_3\text{Cu}_2\text{I}_5$  and green emissive  $\text{Cs}_3\text{Cu}_2\text{Cl}_5$ . (b) Photograph of the pc-LED device operated at a forward bias current of 20 mA. (c) EL spectrum and (d) CIE chromaticity diagram of the LED device.

color observed by the naked eye as shown in Fig. 7(b). The green-yellow emission color was obtained when the pc-LED device operated at a forward bias current of 20 mA. The electroluminescence (EL) spectrum [Fig. 7(c)] of the UV-pumped pc-LED exhibits two peaks: at 479 nm from the blue emissive  $\text{Cs}_3\text{Cu}_2\text{I}_5$  and at 547 nm from green emissive  $\text{Cs}_3\text{Cu}_2\text{Cl}_5$ . The Commission International de l'Éclairage (CIE) color coordinates of the UV-pumped pc-LED are (0.278, 0.383); this is marked in the CIE 1931 color space, and the color points are laid on the green-yellow region near the black-body Planckian locus [Fig. 7(d)].

#### 4. CONCLUSIONS

In summary, we have developed a simple and energy-saving route to synthesize stable lead-free perovskites in a dry ball milling process. The obtained blue emissive  $\text{Cs}_3\text{Cu}_2\text{I}_5$  powder exhibits a high PL QY of 60% with a long lifetime of 1.13  $\mu\text{s}$  and a huge Stokes shift of 137 nm. The luminescence mechanism of  $\text{Cs}_3\text{Cu}_2\text{I}_5$  could be explained by self-trapped excitons that originate from Jahn–Teller distortion of the Cu tetrahedral site. The green emissive  $\text{Cs}_3\text{Cu}_2\text{Cl}_5$  perovskite with PL QY of 53% was successfully fabricated by using the same process for the first time, with the PL peak at 510 nm. We finally realized a UV-pumped LED device by using blue emissive  $\text{Cs}_3\text{Cu}_2\text{I}_5$  and green emissive  $\text{Cs}_3\text{Cu}_2\text{Cl}_5$  as phosphors.

**Funding.** National Key R&D Program of China (2017YFB1002900); National Natural Science Foundation of China (51602024, 61420106014, 61574017, 61775019); Beijing Nova Program (Z171100001117047); Beijing Outstanding Young Scientist Program (BJJWZYJH01201910007022); Opened Fund of the State Key Laboratory on Integrated Optoelectronics (IOSKL2017KF13).

**Disclosures.** The authors declare no conflicts of interest.

†These authors contributed equally to this work.

#### REFERENCES

- Q. A. Akkerman, G. Raino, M. V. Kovalenko, and L. Manna, "Genesis, challenges and opportunities for colloidal lead halide perovskite nanocrystals," *Nat. Mater.* **17**, 394–405 (2018).
- S. Chang, Z. L. Bai, and H. Z. Zhong, "In situ fabricated perovskite nanocrystals: a revolution in optical materials," *Adv. Opt. Mater.* **6**, 1800380 (2018).
- M. V. Kovalenko, L. Protesescu, and M. I. Bodnarchuk, "Properties and potential optoelectronic applications of lead halide perovskite nanocrystals," *Science* **358**, 745–750 (2017).
- N. J. Jeon, J. H. Noh, Y. C. Kim, W. S. Yang, S. Ryu, and S. I. Seok, "Solvent engineering for high-performance inorganic-organic hybrid perovskite solar cells," *Nat. Mater.* **13**, 897–903 (2014).
- C. X. Ran, J. Xi, W. Y. Gao, F. Yuan, T. Lei, B. Jiao, X. Hou, and Z. X. Wu, "Bilateral interface engineering toward efficient 2D-3D bulk heterojunction tin halide lead-free perovskite solar cells," *ACS Energy Lett.* **3**, 713–721 (2018).
- E. M. Sanehira, A. R. Marshall, J. A. Christians, S. P. Harvey, P. N. Ciesielski, L. M. Wheeler, P. Schulz, L. Y. Lin, M. C. Beard, and J. M. Luther, "Enhanced mobility  $\text{CsPbI}_3$  quantum dot arrays for record-efficiency, high-voltage photovoltaic cells," *Sci. Adv.* **3**, eaao4204 (2017).
- J. B. You, L. Meng, T.-B. Song, T.-F. Guo, Y. M. Yang, W.-H. Chang, Z. R. Hong, H. J. Chen, H. P. Zhou, Q. Chen, Y. S. Liu, N. D. Marco, and Y. Yang, "Improved air stability of perovskite solar cells via solution-processed metal oxide transport layers," *Nat. Nanotechnol.* **11**, 75–81 (2016).
- Y. Cao, N. N. Wang, H. Tian, J. S. Guo, Y. Q. Wei, H. Chen, Y. F. Miao, W. Zou, K. Pan, Y. R. He, H. Cao, Y. Ke, M. M. Xu, Y. Wang, M. Yang, K. Du, Z. W. Fu, D. C. Kong, D. X. Dai, Y. Z. Jin, G. Q. Li, H. Li, Q. M. Peng, J. P. Wang, and W. Huang, "Perovskite light-emitting diodes based on spontaneously formed submicrometre-scale structures," *Nature* **562**, 249–253 (2018).
- T. Chiba, S. Ohisa, Y. Hayashi, H. Ebe, K. Hoshi, J. Sato, S. Sato, Y.-J. Pu, S. Ohisa, and J. Kido, "Anion-exchange red perovskite quantum dots with ammonium iodine salts for highly efficient light-emitting devices," *Nat. Photonics* **12**, 681–687 (2018).
- K. B. Lin, J. Xing, L. N. Quan, F. P. G. de Arquer, X. W. Gong, J. X. Lu, L. Q. Xie, W. J. Zhao, D. Zhang, C. Z. Yan, W. Q. Li, X. Y. Liu, Y. Lu, J. Kirman, E. H. Sargent, Q. H. Xiong, and Z. H. Wei, "Perovskite light-emitting diodes with external quantum efficiency exceeding 20 percent," *Nature* **562**, 245–248 (2018).
- M. Lu, Y. Zhang, S. Wang, J. Guo, W. W. Yu, and A. L. Rogach, "Metal halide perovskite light-emitting devices: promising technology for next-generation displays," *Adv. Funct. Mater.* **29**, 1902008 (2019).
- D. B. Han, M. Imran, M. J. Zhang, S. Chang, X. G. Wu, X. Zhang, J. L. Tang, M. S. Wang, S. Ali, X. G. Li, G. Yu, J. B. Han, B. S. Zou, and H. Z. Zhong, "Efficient light-emitting diodes based on *in situ* fabricated  $\text{FaPbBr}_3$  nanocrystals: the enhancing role of the ligand-assisted reprecipitation process," *ACS Nano* **12**, 8808–8816 (2018).
- Y. Liu, J. Y. Cui, K. Du, H. Tian, Z. F. He, Q. H. Zhou, Z. L. Yang, Y. Z. Deng, D. Chen, X. B. Zuo, Y. Ren, L. Wang, H. M. Zhu, B. D. Zhao, D. W. Di, J. P. Wang, R. H. Friend, and Y. Z. Jin, "Efficient blue light-emitting diodes based on quantum-confined bromide perovskite nanostructures," *Nat. Photonics* **13**, 760–767 (2019).
- Z. C. Li, Z. M. Chen, Y. C. Yang, Q. F. Xue, H.-L. Yip, and Y. Cao, "Modulation of recombination zone position for quasi-two-dimensional blue perovskite light-emitting diodes with efficiency exceeding 5%," *Nat. Commun.* **10**, 1027 (2019).
- Y. J. Fang, Q. F. Dong, Y. C. Shao, Y. B. Yuan, and J. S. Huang, "Highly narrowband perovskite single-crystal photodetectors enabled by surface-charge recombination," *Nat. Photonics* **9**, 679–686 (2015).
- M. I. Saidaminov, V. Adinolfi, R. Comin, A. L. Abdelhady, W. Peng, I. Dursun, M. Yuan, S. Hoogland, E. H. Sargent, and O. M. Bakr, "Planar-integrated single-crystalline perovskite photodetectors," *Nat. Commun.* **6**, 8724 (2015).
- L. Wang, L. H. Meng, L. Chen, S. Huang, X. G. Wu, G. Dai, L. G. Deng, J. B. Han, B. S. Zou, C. F. Zhang, and H. Z. Zhong, "Ultralow-threshold and color-tunable continuous-wave lasing at room-temperature from

- in situ* fabricated perovskite quantum dots,” *J. Phys. Chem. Lett.* **10**, 3248–3253 (2019).
18. Y. F. Jia, R. A. Kerner, A. J. Grede, B. P. Rand, and N. C. Giebink, “Continuous-wave lasing in an organic-inorganic lead halide perovskite semiconductor,” *Nat. Photonics* **11**, 784–788 (2017).
  19. Q. Wei, X. J. Li, C. Liang, Z. P. Zhang, J. Guo, G. Hong, G. C. Xing, and W. Huang, “Recent progress in metal halide perovskite micro- and nanolasers,” *Adv. Opt. Mater.* **7**, 1900080 (2019).
  20. B.-W. Park and S. I. Seok, “Intrinsic instability of inorganic-organic hybrid halide perovskite materials,” *Adv. Mater.* **31**, 1805337 (2019).
  21. A. Babayigit, A. Ethirajan, M. Muller, and B. Conings, “Toxicity of organometal halide perovskite solar cells,” *Nat. Mater.* **15**, 247–251 (2016).
  22. A. F. Wang, Y. Y. Guo, F. Muhammad, and Z. T. Deng, “Controlled synthesis of lead-free cesium tin halide perovskite cubic nanocages with high stability,” *Chem. Mater.* **29**, 6493–6501 (2017).
  23. D. H. Fabini, G. Laurita, J. S. Bechtel, C. C. Stoumpos, H. A. Evans, A. G. Kontos, Y. S. Raptis, P. Falaras, A. V. D. Ven, M. G. Kanatzidis, and R. Seshadri, “Dynamic stereochemical activity of the Sn<sup>2+</sup> lone pair in perovskite CsSnBr<sub>3</sub>,” *J. Am. Chem. Soc.* **138**, 11820–11832 (2016).
  24. B. M. Benin, D. N. Dirin, V. Morad, M. Wçrle, S. Yakunin, G. Rainò, O. Nazarenko, M. Fischer, I. Infante, and M. V. Kovalenko, “Highly emissive self-trapped excitons in fully inorganic zero dimensional tin halides,” *Angew. Chem.* **130**, 11499–11503 (2018).
  25. X. Zhang, C. Wang, Y. Zhang, X. Zhang, S. Wang, M. Lu, H. Cui, S. V. Kershaw, W. W. Yu, and A. L. Rogach, “Bright orange electroluminescence from lead-free two-dimensional perovskites,” *ACS Energy Lett.* **4**, 242–248 (2019).
  26. J.-T. Lin, C.-C. Liao, C.-S. Hsu, D.-G. Chen, H.-M. Chen, M.-K. Tsai, P.-T. Chou, and C.-W. Chiou, “Harnessing dielectric confinement on tin perovskites to achieve emission quantum yield up to 21%,” *J. Am. Chem. Soc.* **141**, 10324–10330 (2019).
  27. M. Y. Leng, Y. Yang, K. Zeng, Z. W. Chen, Z. F. Tan, S. R. Li, J. H. Li, B. Xu, D. B. Li, M. P. Hautzinger, Y. P. Fu, T. Y. Zhai, L. Xu, G. D. Niu, S. Jin, and J. Tang, “All-inorganic bismuth-based perovskite quantum dots with bright blue photoluminescence and excellent stability,” *Adv. Funct. Mater.* **28**, 1704446 (2017).
  28. B. Yang, J. S. Chen, F. Hong, X. Mao, K. B. Zheng, S. Q. Yang, Y. J. Li, T. Pullerits, W. Q. Deng, and K. L. Han, “Lead-free, air-stable all-inorganic cesium bismuth halide perovskite nanocrystals,” *Angew. Chem. (Int. Ed.)* **56**, 12471–12475 (2017).
  29. M. Leng, Y. Yang, Z. Chen, W. Gao, J. Zhang, G. Niu, D. Li, H. Song, J. Zhang, S. Jin, and J. Tang, “Surface passivation of bismuth-based perovskite variant quantum dots to achieve efficient blue emission,” *Nano Lett.* **18**, 6076–6083 (2018).
  30. Y. Bekenstein, J. C. Dahl, J. M. Huang, W. T. Osowiecki, J. K. Swabeck, E. M. Chan, P. D. Yang, and A. P. Alivisatos, “The making and breaking of lead-free double perovskite nanocrystals of cesium silver-bismuth halide compositions,” *Nano Lett.* **18**, 3502–3508 (2018).
  31. Q. Li, Y. G. Wang, W. C. Pan, W. G. Yang, B. Zou, J. Tang, and Z. W. Quan, “High-pressure band-gap engineering in lead-free Cs<sub>2</sub>AgBiBr<sub>6</sub> double perovskite,” *Angew. Chem. (Int. Ed.)* **56**, 15969–15973 (2017).
  32. L. Zhou, J. F. Liao, Z. G. Huang, J. H. Wei, X. D. Wang, W. G. Li, H. Y. Chen, D. B. Kuang, and C. Y. Su, “A highly red-emissive lead-free indium-based perovskite single crystal for sensitive water detection,” *Angew. Chem. (Int. Ed.)* **58**, 5277–5281 (2019).
  33. L. Zhou, J. F. Liao, Z. G. Huang, J. H. Wei, X. D. Wang, H. Y. Chen, and D. B. Kuang, “Intrinsic self-trapped emission in 0D lead-free (C<sub>4</sub>H<sub>14</sub>N<sub>2</sub>)<sub>2</sub>In<sub>2</sub>Br<sub>10</sub> single crystal,” *Angew. Chem. (Int. Ed.)* **58**, 2–8 (2019).
  34. F. Umar, J. Zhang, Z. X. Jin, I. Muhammad, X. K. Yang, H. Deng, K. Jahangeer, Q. S. Hu, H. S. Song, and J. Tang, “Dimensionality controlling of Cs<sub>3</sub>Sb<sub>2</sub>I<sub>9</sub> for efficient all-inorganic planar thin film solar cells by HCl-assisted solution method,” *Adv. Opt. Mater.* **7**, 1801368 (2019).
  35. J. Zhang, Y. Yang, H. Deng, U. Farooq, X. Yang, J. Khan, J. Tang, and H. Song, “High quantum yield blue emission from lead-free inorganic antimony halide perovskite colloidal quantum dots,” *ACS Nano* **11**, 9294–9302 (2017).
  36. X. T. Wu, W. D. Song, Q. Li, X. X. Zhao, D. S. He, and Z. W. Quan, “Synthesis of lead-free CsGeI<sub>3</sub> perovskite colloidal nanocrystals and electron beam-induced transformations,” *Chem. Asian J.* **13**, 1654–1659 (2018).
  37. P. F. Cheng, T. Wu, J. W. Zhang, Y. J. Li, J. X. Liu, L. Jiang, X. Mao, R. F. Lu, W. Q. Deng, and K. L. Han, “(C<sub>6</sub>H<sub>5</sub>C<sub>2</sub>H<sub>4</sub>NH<sub>3</sub>)<sub>2</sub>GeI<sub>4</sub>: a layered two-dimensional perovskite with potential for photovoltaic applications,” *J. Phys. Chem. Lett.* **8**, 4402–4406 (2017).
  38. D. Cortecchia, H. A. Dewi, J. Yin, A. Bruno, S. Chen, T. Baikie, P. P. Boix, M. Grätzel, S. Mhaisalkar, C. Soci, and N. Mathews, “Lead-free Ma<sub>2</sub>CuCl<sub>4</sub>Br<sub>4-x</sub> hybrid perovskites,” *Inorg. Chem.* **55**, 1044–1052 (2016).
  39. P. F. Cheng, L. Sun, L. Feng, S. Q. Yang, Y. Yang, D. Y. Zheng, Y. Zhao, Y. B. Sang, R. L. Zhang, D. H. Wei, W. Q. Deng, and K. L. Han, “Colloidal synthesis and optical properties of all-inorganic low-dimensional cesium copper halide nanocrystals,” *Angew. Chem. (Int. Ed.)* **131**, 16233–16237 (2019).
  40. T. Jun, K. Sim, S. Iimura, M. Sasase, H. Kamioka, J. Kim, and H. Hosono, “Lead-free highly efficient blue-emitting Cs<sub>3</sub>Cu<sub>2</sub>I<sub>5</sub> with 0D electronic structure,” *Adv. Mater.* **30**, 1804547 (2018).
  41. T. Li, X. M. Mo, C. Y. Peng, Q. C. Lu, C. J. Qi, X. M. Tao, Y. Ouyang, and Y. L. Zhou, “Distinct green electroluminescence from lead-free CsCuBr<sub>2</sub> halide micro-crosses,” *Chem. Commun.* **55**, 4554–4557 (2019).
  42. R. Rocanova, A. Yangui, H. Nhaili, H. L. Shi, M. H. Du, and B. Saparov, “Near-unity photoluminescence quantum yield in blue-emitting Cs<sub>3</sub>Cu<sub>2</sub>Br<sub>5-x</sub>I<sub>x</sub> (0 ≤ x ≤ 5),” *ACS Appl. Electron. Mater.* **1**, 269–274 (2019).
  43. E. P. Booker, J. T. Griffiths, L. Eyre, C. Ducati, N. C. Greenham, and N. J. L. K. Davis, “Synthesis, characterization, and morphological control of Cs<sub>2</sub>CuCl<sub>4</sub> nanocrystals,” *J. Phys. Chem. C* **123**, 16951–16956 (2019).
  44. P. Yang, G. N. Liu, B. D. Liu, X. D. Liu, Y. B. Lou, J. X. Chen, and Y. X. Zhao, “All-inorganic Cs<sub>2</sub>CuX<sub>4</sub> (X = Cl, Br, and Br/I) perovskite quantum dots with blue-green luminescence,” *Chem. Commun.* **54**, 11638–11641 (2018).
  45. S. Thapa, G. C. Adhikari, H. Y. Zhu, A. Grigoriev, and P. F. Zhu, “Zn-alloyed all-inorganic halide perovskite-based white light-emitting diodes with superior color quality,” *Sci. Rep.* **9**, 1 (2019).
  46. G. C. Adhikari, S. Thapa, H. Zhu, and P. F. Zhu, “Mg<sup>2+</sup>-alloyed all-inorganic halide perovskites for white light-emitting diodes by 3D-printing method,” *Adv. Opt. Mater.* **7**, 1900916 (2019).
  47. Q. Hu, Z. Li, Z. Tan, H. Song, C. Ge, G. Niu, J. Han, and J. Tang, “Rare earth ion-doped CsPbBr<sub>3</sub> nanocrystals,” *Adv. Opt. Mater.* **6**, 1700864 (2018).
  48. R. A. Sheldon, “Green solvents for sustainable organic synthesis: state of the art,” *Green Chem.* **7**, 267–278 (2005).
  49. F. Gomollón-Bel, “Ten chemical innovations that will change our world: IUPAC identifies emerging technologies in chemistry with potential to make our planet more sustainable,” *Chem. Int.* **41**, 12–17 (2019).
  50. D. Prochowicz, M. Sasaki, P. Yadav, M. Grätzel, and J. Lewinski, “Mechanoperovskites for photovoltaic applications: preparation, characterization, and device fabrication,” *Acc. Chem. Res.* **52**, 3233–3243 (2019).
  51. Z. Y. Zhu, Q. Q. Yang, L. F. Gao, L. Zhang, A. Y. Shi, C. L. Sun, Q. Wang, and H. L. Zhang, “Solvent-free mechanosynthesis of composition-tunable cesium lead halide perovskite quantum dots,” *J. Phys. Chem. Lett.* **8**, 1610–1614 (2017).
  52. L. Protesescu, S. Yakunin, O. Nazarenko, D. N. Dirin, and M. V. Kovalenko, “Low-cost synthesis of highly luminescent colloidal lead halide perovskite nanocrystals by wet ball milling,” *ACS Appl. Nano Mater.* **1**, 1300–1308 (2018).
  53. D. Q. Chen, J. N. Li, X. Chen, J. K. Chen, and J. S. Zhong, “Grinding synthesis of APbX<sub>3</sub> (A = Ma, Fa, Cs; X = Cl, Br, I) perovskite nanocrystals,” *ACS Appl. Mater. Interfaces* **11**, 10059–10067 (2019).
  54. J. J. Luo, X. M. Wang, S. R. Li, J. Liu, Y. M. Guo, G. D. Niu, L. Yao, Y. H. Fu, L. Gao, Q. S. Dong, C. Y. Zhao, M. Y. Leng, F. S. Ma, W. X. Liang, L. D. Wang, S. Y. Jin, J. B. Han, L. J. Zhang, J. Etheridge, J. B. Wang, Y. F. Yan, E. H. Sargent, and J. Tang, “Efficient and stable

- emission of warm-white light from lead-free halide double perovskites," *Nature* **563**, 541–545 (2018).
55. Z. Yuan, C. K. Zhou, Y. Tian, Y. Shu, J. Messier, J. C. Wang, L. J. van de Burgt, K. Kountouriotis, Y. Xin, E. Holt, K. Schanze, R. Clark, T. Siegrist, and B. W. Ma, "One-dimensional organic lead halide perovskites with efficient bluish white-light emission," *Nat. Commun.* **8**, 14051 (2017).
  56. S. Seth and A. Samanta, "Photoluminescence of zero-dimensional perovskites and perovskite-related materials," *J. Phys. Chem. Lett.* **9**, 176–183 (2018).
  57. B. T. Diroll, G. Nedelcu, M. V. Kovalenko, and R. D. Schaller, "High-temperature photoluminescence of CsPbX<sub>3</sub> (X = Cl, Br, I) nanocrystals," *Adv. Funct. Mater.* **27**, 1606750 (2017).
  58. R. An, F. Y. Zhang, X. S. Zou, Y. Y. Tang, M. L. Liang, I. Oshchapovskyy, Y. C. Liu, A. Honarfar, Y. Q. Zhong, C. S. Li, H. F. Geng, J. S. Chen, S. E. Canton, T. N. Pullerits, and K. B. Zheng, "Photostability and photodegradation processes in colloidal CsPbI<sub>3</sub> perovskite quantum dots," *ACS Appl. Mater. Interfaces* **10**, 39222–39227 (2018).
  59. M. Y. Gao, C. Zhang, L. Y. Lian, J. W. Guo, Y. Xia, F. Pan, X. M. Su, J. B. Zhang, H. L. Li, and D. L. Zhang, "Controlled synthesis and photostability of blue emitting Cs<sub>3</sub>Bi<sub>2</sub>Br<sub>9</sub> perovskite nanocrystals by employing weak polar solvents at room temperature," *J. Mater. Chem. C* **7**, 3688–3695 (2019).
  60. C. Zhou, H. Lin, Q. He, L. Xu, M. Worku, M. Chaaban, S. Lee, X. Shi, M.-H. Du, and B. Ma, "Low dimensional metal halide perovskites and hybrids," *Mater. Sci. Eng. R* **137**, 38–65 (2019).
  61. G. D. Niu, W. Z. Li, F. Q. Meng, L. D. Wang, H. P. Dong, and Y. Qiu, "Study on the stability of CH<sub>3</sub>NH<sub>3</sub>PbI<sub>3</sub> films and the effect of post-modification by aluminum oxide in all-solid-state hybrid solar cells," *J. Mater. Chem. A* **2**, 705–710 (2014).
  62. T. Zhang, M. I. Dar, G. Li, F. Xu, N. Guo, M. Grätzel, and Y. Zhao, "Bication lead iodide 2D perovskite component to stabilize inorganic  $\alpha$ -CsPbI<sub>3</sub> perovskite phase for high-efficiency solar cells," *Sci. Adv.* **3**, e1700841 (2017).
  63. S. Hull and P. Berastegui, "Crystal structures and ionic conductivities of ternary derivatives of the silver and copper monohalides-II: ordered phases within the (AgX)<sub>x</sub>(MX)<sub>1-x</sub> and (CuX)<sub>x</sub>(MX)<sub>1-x</sub> (M=K, Rb and Cs; X=Cl, Br and I) systems," *J. Solid State Chem.* **177**, 3156–3173 (2004).
  64. A. Verma, D. P. Jaihindh, and Y.-P. Fu, "Photocatalytic 4-nitrophenol degradation and oxygen evolution reaction in CuO/g-C<sub>3</sub>N<sub>4</sub> composites prepared by deep eutectic solvent-assisted chlorine doping," *Dalton Trans.* **48**, 8594–8610 (2019).
  65. L. G. Liu, H. Z. Zhong, Z. L. Bai, T. Zhang, W. P. Fu, L. J. Shi, H. Y. Xie, L. G. Deng, and B. S. Zou, "Controllable transformation from rhombohedral Cu<sub>1.8</sub>S nanocrystals to hexagonal CuS clusters: phase- and composition-dependent plasmonic properties," *Chem. Mater.* **25**, 4828–4834 (2013).
  66. N. F. Mott and A. M. Stoneham, "The lifetime of electrons, holes and excitons before self-trapping," *J. Phys. C* **10**, 3391–3398 (1977).
  67. Z. Luo, Q. Li, L. Zhang, T. L. Wu, C. Zou, Y. Liu, and Z. Quan, "0D Cs<sub>3</sub>Cu<sub>2</sub>X<sub>5</sub> (X = I, Br, and Cl) nanocrystals: colloidal syntheses and optical properties," *Small* **16**, 1905226 (2019).
  68. R. L. Zhang, X. Mao, Y. Yang, S. Q. Yang, W. Y. Zhao, T. Wumaier, D. H. Wei, W. Q. Deng, and K. L. Han, "Air-stable, lead-free zero-dimensional mixed bismuth-antimony perovskite single crystals with ultrabroadband emission," *Angew. Chem.* **131**, 2751–2755 (2019).